

Supplementary Information

Video-rate nanoscopy using sCMOS camera-specific single-molecule localization algorithms

Fang Huang¹, Tobias M. P. Hartwich^{1,2,3,9}, Felix E. Rivera-Molina^{1,9}, Yu Lin^{4,5}, Whitney C. Duim¹, Jane J. Long⁶, Pradeep D. Uchil⁷, Jordan R. Myers¹, Michelle A. Baird⁸, Walther Mothes⁷, Michael W. Davidson⁸, Derek Toomre¹ and Joerg Bewersdorf^{1,4,5,*}

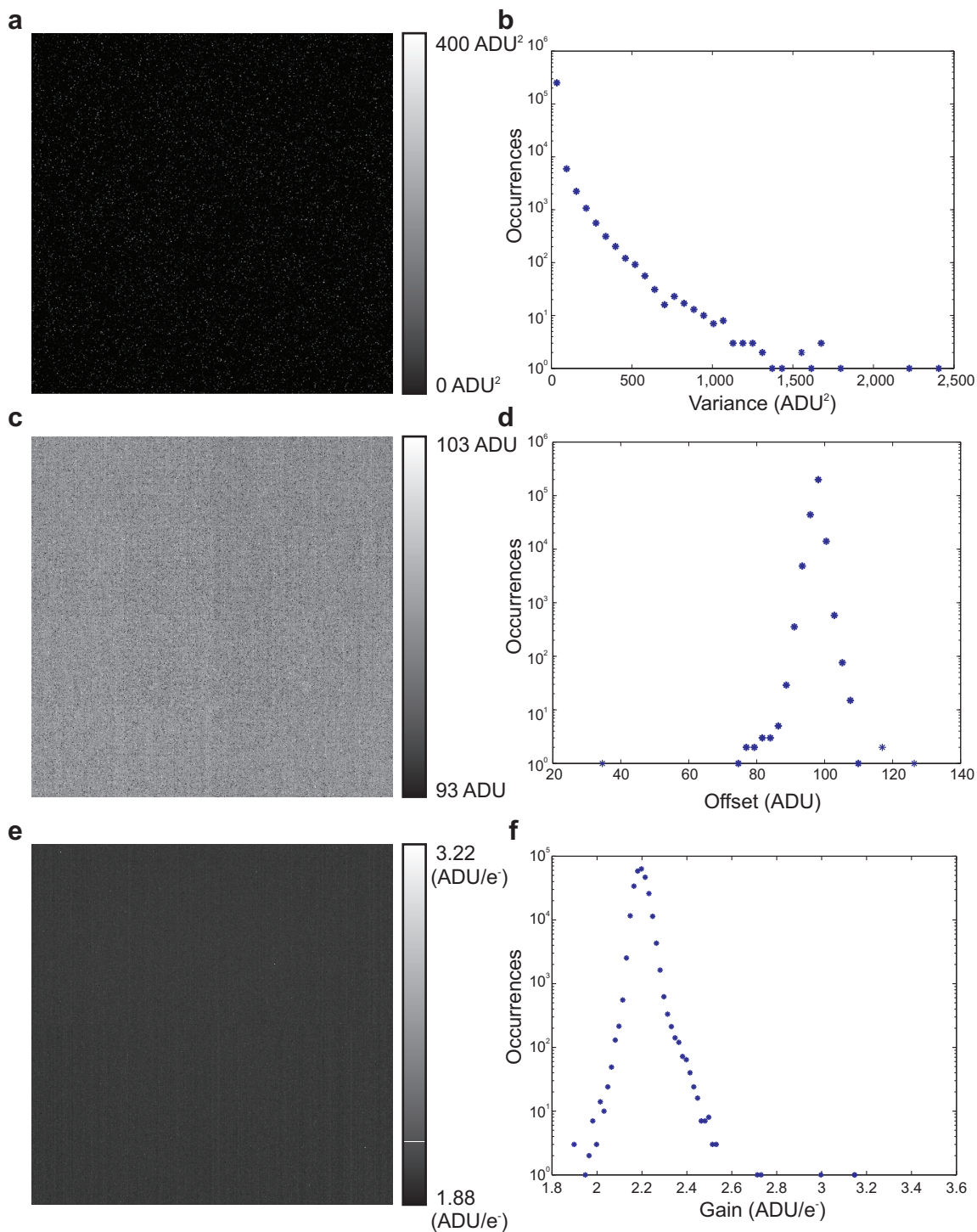
1. Department of Cell Biology, Yale University School of Medicine, New Haven, CT 06520, USA
2. Department of Biophysical Chemistry, University of Heidelberg, 69120 Heidelberg, Germany
3. Department of New Materials and Biosystems, Max Planck Institute for Intelligent Systems, 70569 Stuttgart, Germany
4. Department of Biomedical Engineering, Yale University, New Haven, CT 06520, USA
5. Integrated Graduate Program in Physical and Engineering Biology, Yale University, New Haven, CT 06520, USA
6. Yale College, Yale University, New Haven, CT 06520, USA
7. Department of Microbial Pathogenesis, Yale University School of Medicine, New Haven, CT 06520, USA
8. National High Magnetic Field Laboratory and Department of Biological Science, Florida State University, Tallahassee, FL 32310, USA
9. These authors contributed equally to this work

*Correspondence to: Joerg Bewersdorf email: joerg.bewersdorf@yale.edu

Supplementary Items	Title
Supplementary Figure 1	Maps and histograms of the pixel-dependent noise characteristics
Supplementary Figure 2	Diagram of single-molecule localization-based super-resolution analysis steps for EMCCD and sCMOS
Supplementary Figure 3	Komogonov distance comparison between Poisson and the analytical approximation of sCMOS noise
Supplementary Figure 4	Demonstration of readout noise introduced biases
Supplementary Figure 5	Performance comparison between MLE and MLE _{sCMOS} on simulated microtubules
Supplementary Figure 6	Simplified schematic of custom-built setup with both an EMCCD and a sCMOS camera
Supplementary Figure 7	Relative improvement in localization precision (decrease in localization uncertainty) predicted by CRLB and CRLB _{sCMOS} for

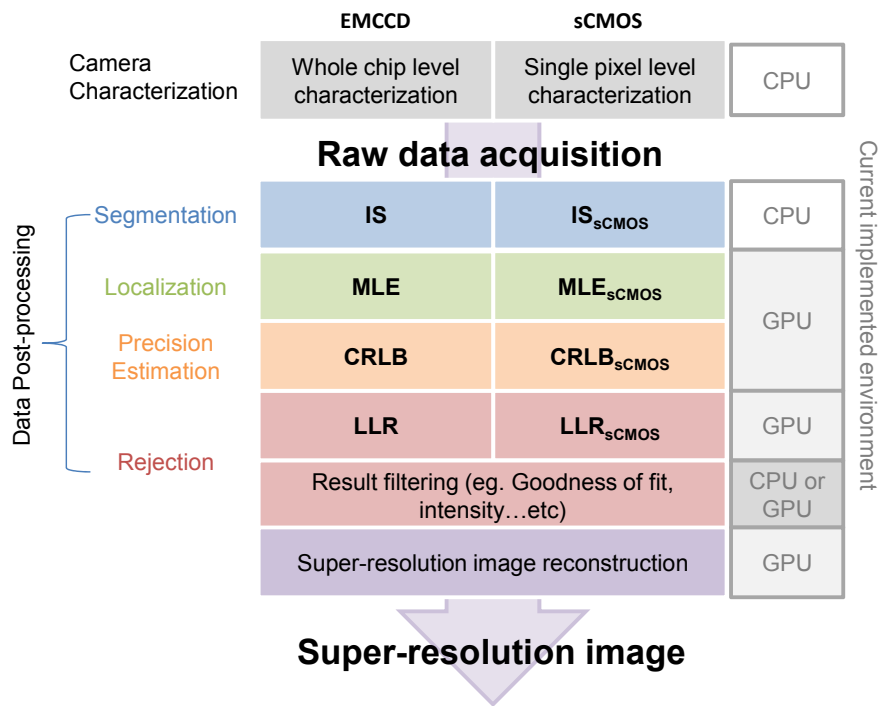
	EMCCD and sCMOS cameras respectively
Supplementary Figure 8	Localization precision and effective photon number comparison for a single bead imaged by sCMOS and EMCCD cameras
Supplementary Figure 9	Localization precision histograms for Fig. 2a and Fig 2e-g
Supplementary Figure 10	Focal adhesion super-resolution image recorded in 3 seconds
Supplementary Figure 11	Super-resolution image of mEos3.2-labeled clathrin-coated pits (CCPs) in a HeLa cell
Supplementary Figure 12	Super-resolution imaging of EB3-mEos3.2 in a live HeLa cell
Supplementary Figure 13	Nyquist resolution measure for the 31-ms super-resolution images shown in Fig. 4
Supplementary Table	Primers used in the study
Supplementary Note	
Supplementary Video 1	Super-resolution video of mEOS3.2-labeled clathrin coated pits in a live HeLa cell
Supplementary Video 2	Super resolution video of mEOS3.2-labeled clathrin coated pits in a second live HeLa cell
Supplementary Video 3	Super resolution video for a small cutout of a larger data set of mEOS3.2-labeled clathrin coated pits in a live HeLa cell
Supplementary Video 4	Super resolution video for a small cutout of a larger data set of mEOS3.2-labeled clathrin coated pits in a live HeLa cell
Supplementary Video 5	Super resolution video for a small cutout of a larger data set of mEOS3.2-labeled clathrin coated pits in a live HeLa cell
Supplementary Video 6	Super resolution video of tdEos-labeled Human pyruvate dehydrogenase alpha 1 (PDHA1) in COS-7 cells
Supplementary Video 7	Super resolution video of mEOS3.2 labeled EB3 in live HeLa cells
Supplementary Video 8	Super resolution video of tdEos-labeled peroxisome membrane protein in live COS-7 cells
Supplementary Video 9	Super resolution video of Alexa Fluor 647-labeled transferrin receptor cluster dynamics as shown in Fig. 4a
Supplementary Video 10	Super resolution video of Alexa Fluor 647-labeled transferrin receptor cluster dynamics as shown in Fig. 4b
Supplementary Data	Zip-archive of obtained localization estimates and uncompressed super-resolution images for Fig. 2a. (1) Uncompressed super-resolution image stretched for visualization purpose. (2) Uncompressed 2D histogram image. (3) List of Localization estimates containing x, y position estimates and their averaged localization uncertainty (square root of their mean variance from CRLBsCMOS). Units are in pixels (103 nm).
Supplementary Software	Example of the developed algorithms implemented in MATLAB and CUDA.

Supplementary Figure 1: Maps and histograms of the pixel-dependent noise characteristics



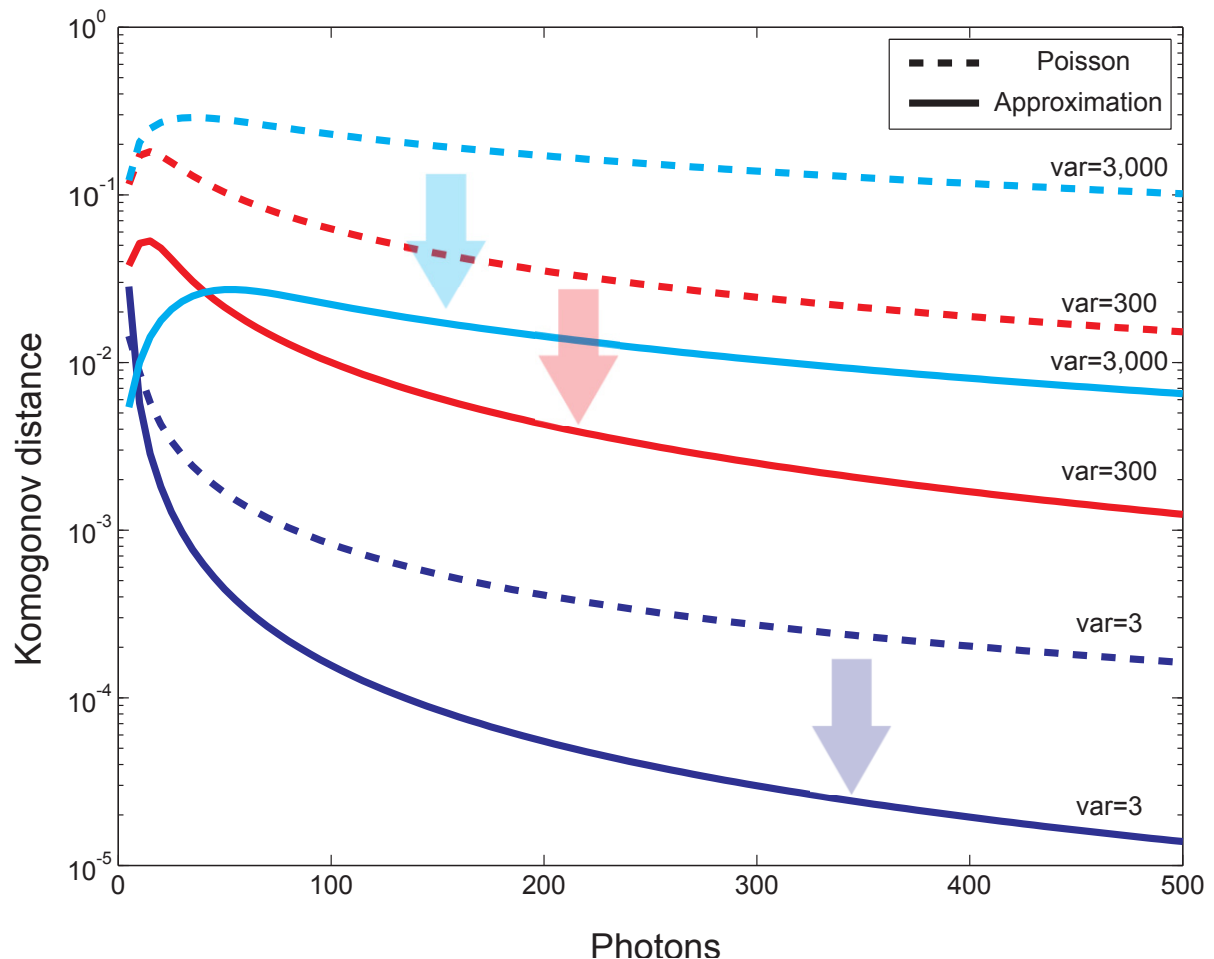
Supplementary Figure 1: Maps and histograms of the pixel-dependent noise characteristics (pixel variance, offset and gain) in a 512×512 pixel sub-region centered on the sCMOS chip of a Hamamatsu ORCA Flash 4.0 camera. (a, c, e) Noise variance (a), offset (c) and gain (e) values for each pixel. (b, d, f) Histograms of the variance, offset and gain values, respectively. The vertical stripe pattern in the obtained amplification gain map in (e) reflects the column-wise amplifier design of the sCMOS architecture.

Supplementary Figure 2: Diagram of single-molecule localization-based super-resolution analysis steps for EMCCD and sCMOS



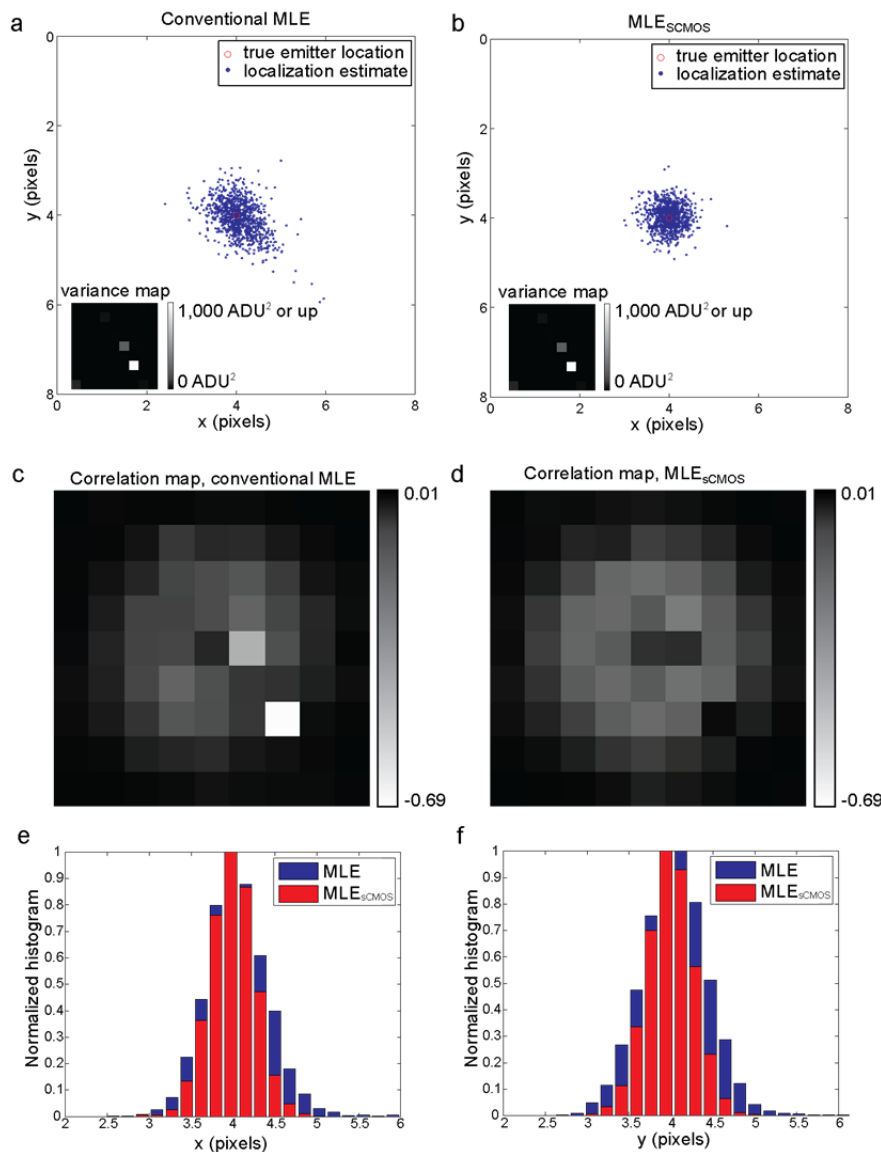
Supplementary Figure 2: Diagram of single-molecule localization-based super-resolution analysis steps for EMCCD and sCMOS. Based on the underlying computing demands and their computational complexities, the processing environment (CPU or GPU) is suggested for each step to shorten analysis time. IS - image segmentation; MLE – maximum likelihood estimation; CRLB – Cramér-Rao lower bound; LLR – log-likelihood ratio.

Supplementary Figure 3: Komogonov distance comparison between Poisson and the analytical approximation of sCMOS noise



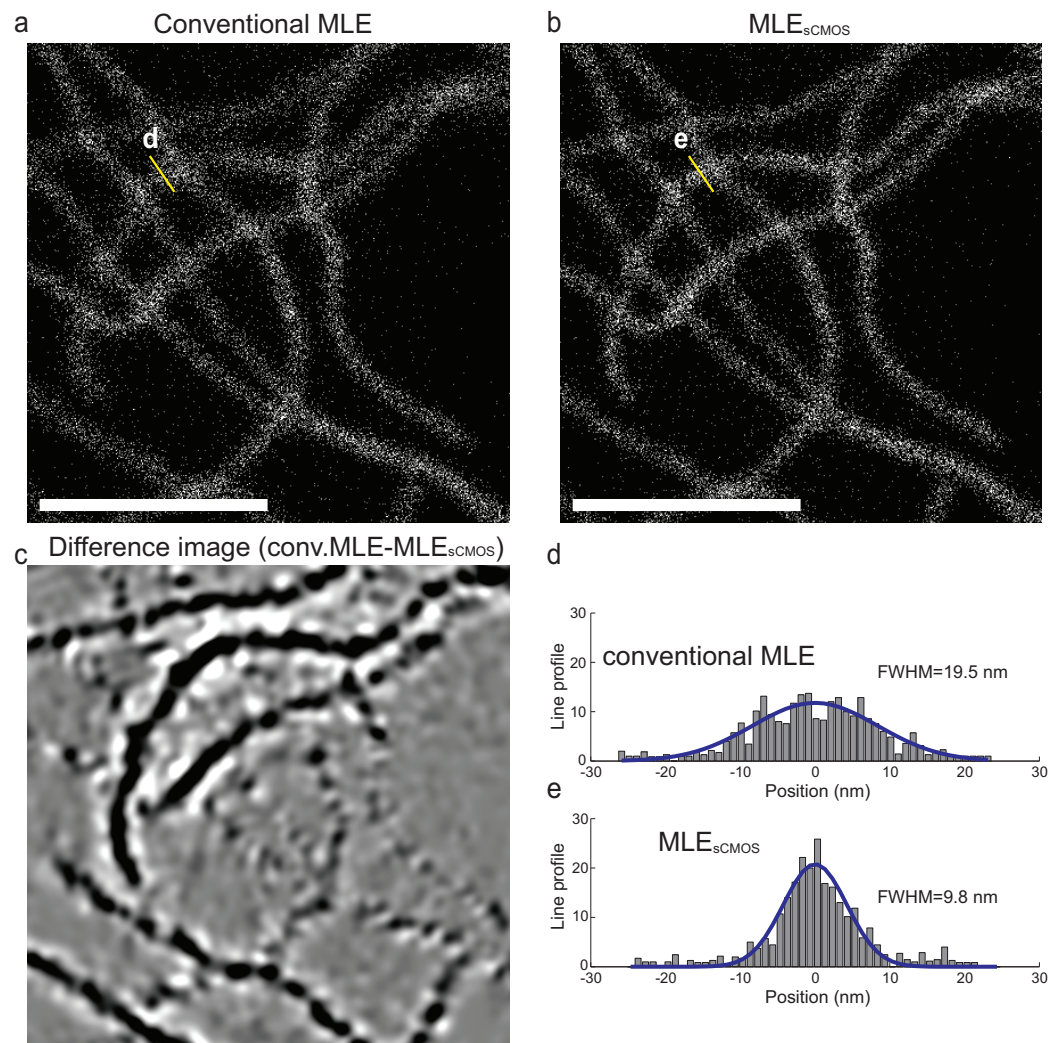
Supplementary Figure 3: Komogonov distance between a Poisson distribution and the convolution distribution (Supplementary Note, Eq. 1.1) (**dashed lines**) and between the developed analytical approximation (Supplementary Note, Eq. 3.3) and the convolution distribution (**solid line**). Comparisons were made at various pixel variance levels over a range of expected detected photon levels per pixel. The Komogonov distance was calculated as the maximum deviation between the two cumulative distribution functions of the tested distributions.

Supplementary Figure 4: Demonstration of readout noise introduced biases



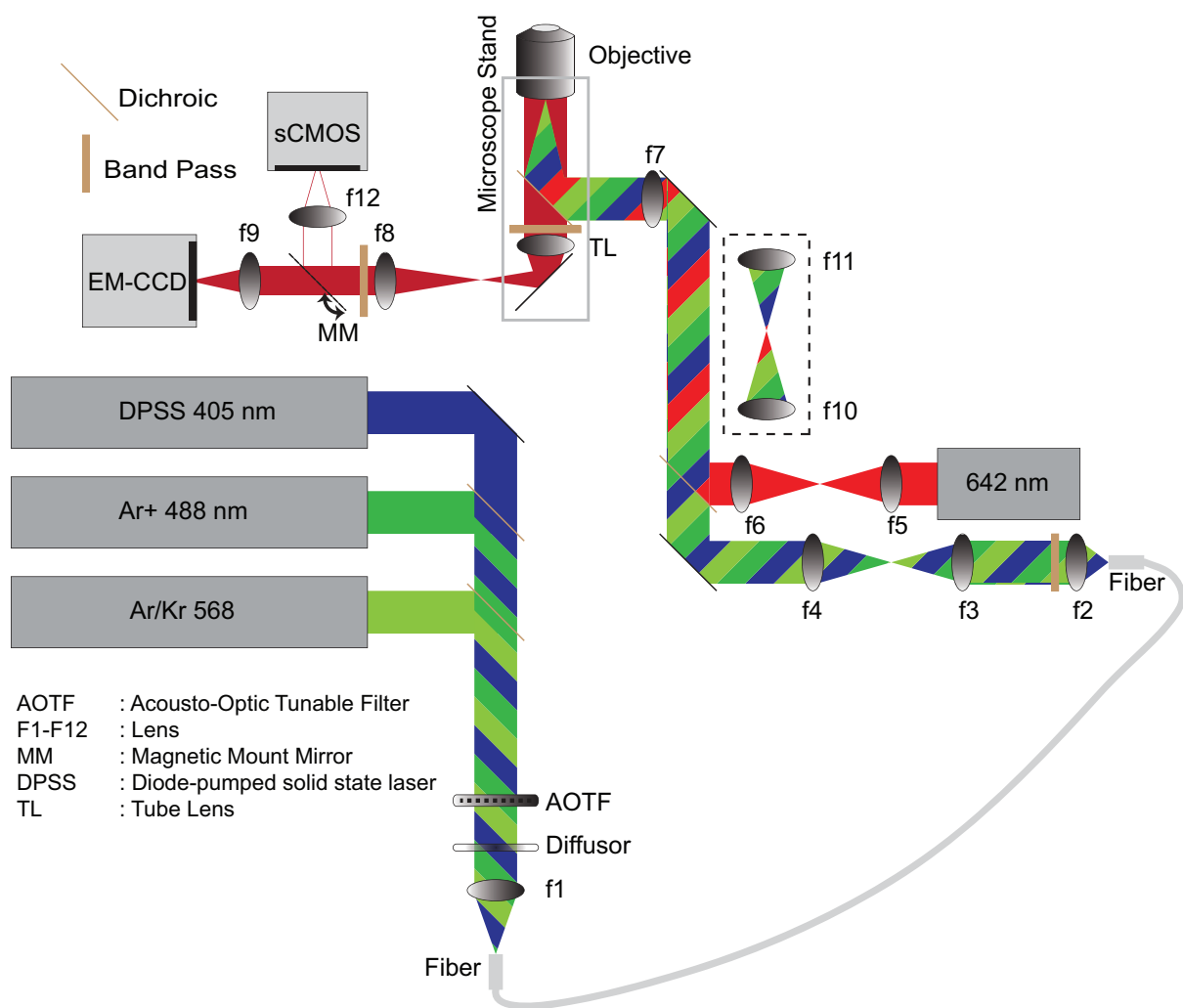
Supplementary Figure 4: Demonstration of readout noise-introduced biases. (a) Scatter plot of the localization estimates for a simulated single emitter detected by a sCMOS camera analyzed with a conventional MLE method¹. The result shows strong biases introduced by high-noise pixels (see inset). (b) Scatter plot of the same data analyzed with MLE_{scmos}. Note the absence of bias. (c) Pixel map of the Pearson correlation coefficient² between the intensity of each pixel and the distance from the pixel to the localization estimates for each frame using conventional MLE. An undesired strong negative correlation between the intensity of high variance pixels and the localization estimates is illustrated by the bright pixels which coincide perfectly with the bright pixels in the variance map in the inset in (a). (d) Same as (c) for MLE_{scmos}. MLE_{scmos} eliminates the strong correlation and results in unbiased estimates shown in (b). The brighter pixels in the correlation map indicate stronger dependence of the localization estimate on the respective pixel value and correspond to the part with steepest slope of the used point-spread function. (e, f) Histograms of localization estimates of both x, y directions. MLE_{scmos} results in higher localization precisions in the absence of biases.

Supplementary Figure 5: Performance comparison between MLE and $\text{MLE}_{\text{sCMOS}}$ on simulated microtubules



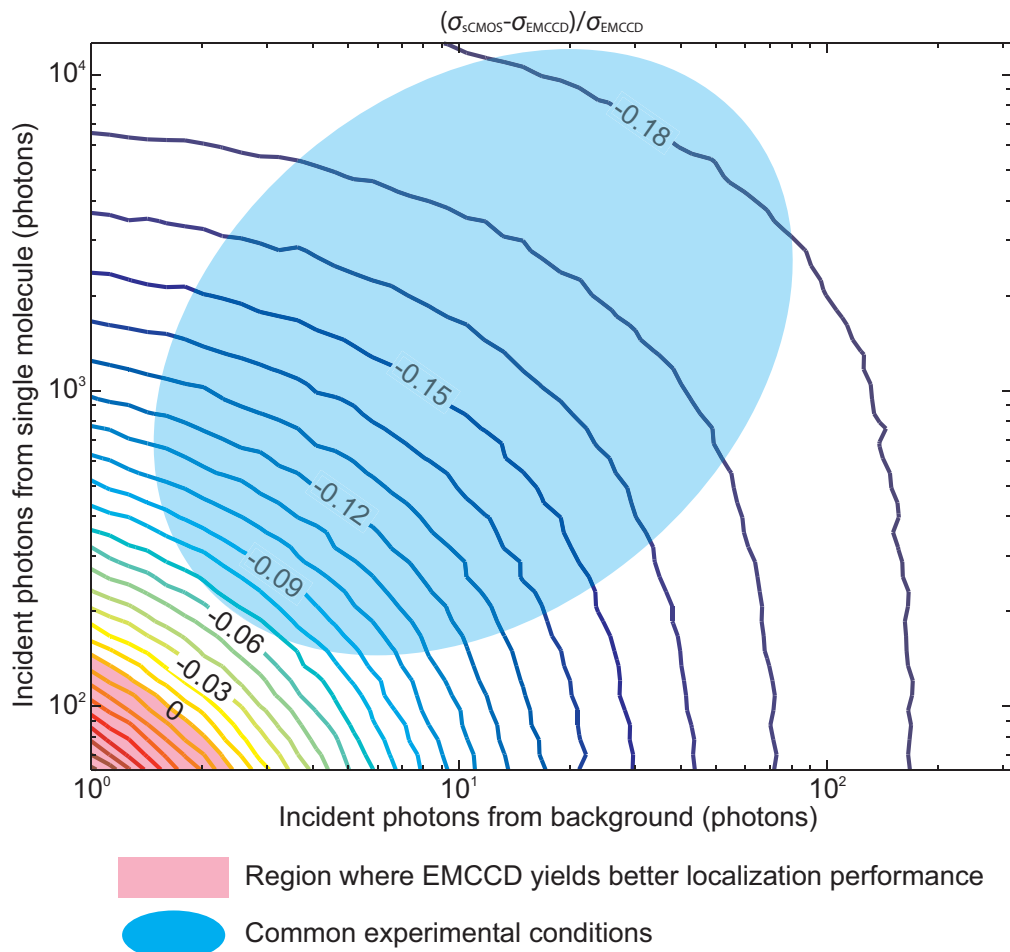
Supplementary Figure 5: Performance comparison between MLE and $\text{MLE}_{\text{sCMOS}}$ on simulated microtubules. (a, b) 2D histogram images of localization estimates from conventional MLE and $\text{MLE}_{\text{sCMOS}}$, respectively. (c) Gaussian-smoothed difference image from (a) and (b). (d, e) Line profiles (integration width of 20 nm) of microtubule structures shown in (a) and (b), respectively. A similar effect in the difference image as is in Fig. 1j can be observed in (c) showing dark lines with bright halos. This is correlated to a ~2-fold improvement in resolution as observed in (d, e). Microtubule structures were simulated using a worm-like chain model.³ Histogram images were generated with a pixel size of 1 nm, where each pixel value represents the number of localization estimates in the pixel. Single emitters were simulated with 1,200 photons per molecule incident on the camera while all the other parameters remained the same as in Fig. 1b. Images were generated first with Poisson noise and then pixel-dependent readout noise was added to each pixel with the noise and gain characteristics of each pixel being obtained from a sub-region of our sCMOS camera. The noise mapping method ensured realistic simulation of sCMOS noise behavior. The difference image was generated similarly to Fig. 1j,k (Online Methods), while the Gaussian smoothing kernel had a standard deviation of 5 nm. Scale bar: 500 nm.

Supplementary Fig. 6: Simplified schematic of custom-built setup with both an EMCCD and a sCMOS camera



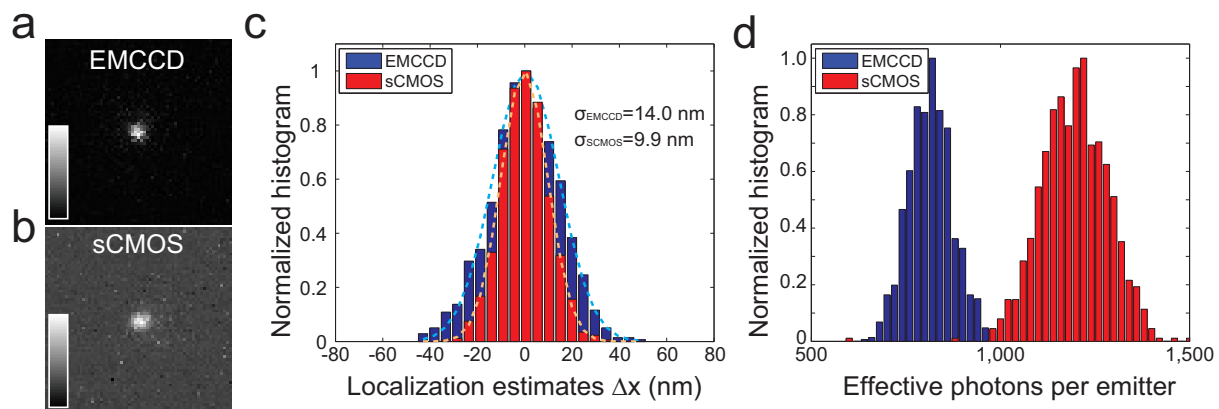
Supplementary Figure 6: Simplified schematic of custom-built setup with both an EMCCD and a sCMOS camera. Beams from a 405 nm laser (Crystalaser), a 488 nm laser (Innova 70, Coherent) and a 568 nm laser (Innova 300, Coherent) are combined and sent through an acousto-optical tunable filter (AOTFnC-400.650-TN, AA Opto-Electronic) and a diffusor before coupled into a multimode fiber. The fiber output is combined with the laser beam of a 642 nm fiber laser (500 mW, MPB Communications) and coupled into the objective (alpha Plan-Apochromat 100x/1.46 Oil DIC, Zeiss) of an inverted microscope stand (Axio Observer D1, Zeiss) for widefield illumination. An optional 2x telescope (lenses f10 and f11) can be added in the excitation beam path to change the size of the illuminated spot in the sample. The emitted fluorescence is collected by the objective and separated from the excitation light by a dichroic mirror (Di01-R405/488/561/635, Semrock) and two bandpass filters (FF01-446/523/600/677 and BLP01-635R-25, Semrock) before being focused onto either an EMCCD (DU897DCS-BV, Andor Technology) or a sCMOS (Orca Flash 4.0, Hamamatsu) camera. Relay optics (lenses f8, f9, f12) are chosen to realize camera pixel sizes corresponding to ~100 nm in the sample.

Supplementary Figure 7: Relative improvement in localization precision (decrease in localization uncertainty) predicted by CRLB and $\text{CRLB}_{\text{sCMOS}}$ for EMCCD and sCMOS cameras, respectively



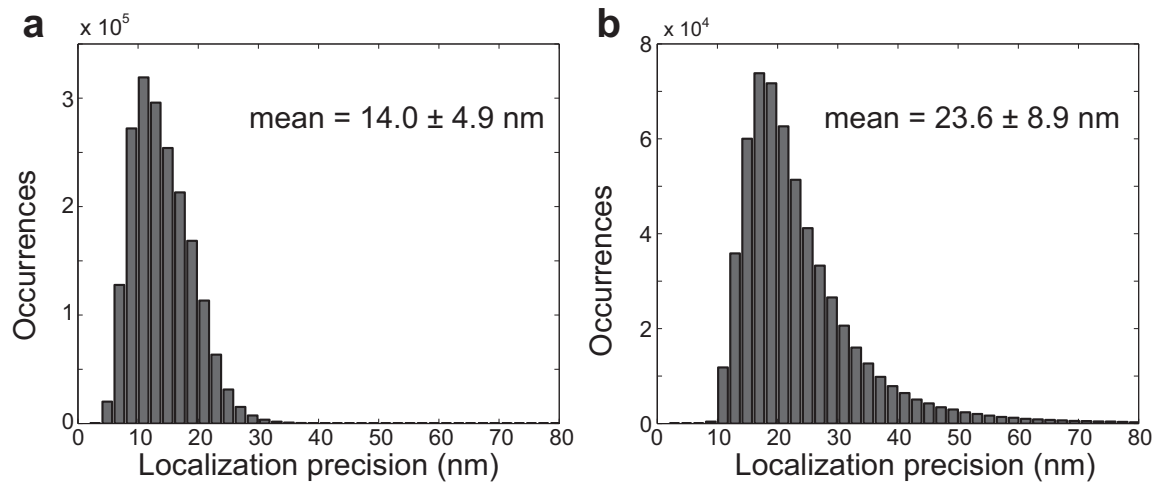
Supplementary Figure 7: Relative improvement in localization precision (decrease in localization uncertainty) predicted by CRLB and $\text{CRLB}_{\text{sCMOS}}$ for EMCCD cameras and sCMOS, respectively. At each incident photon level of background and emitter, CRLB and $\text{CRLB}_{\text{sCMOS}}$ were calculated for each of the 1,000 single emitters ($\sigma_{\text{PSF}}=1.2$, assuming 103 nm square pixels) distributed randomly across the EMCCD and sCMOS camera chip. The calculations are based on the noise and gain characteristics of each pixel of our sCMOS camera in a 512x512 ROI centered in the middle of the camera (Online Methods). The average localization uncertainties for a specific photon and background level, σ_{sCMOS} and σ_{EMCCD} , were calculated by averaging all uncertainties obtained from position estimates of the 1,000 emitters. Effective quantum efficiencies in EMCCD and sCMOS simulations were 48% and 73%, respectively.

Supplementary Figure 8: Localization precision and effective photon comparison for a single bead imaged by sCMOS and EMCCD cameras



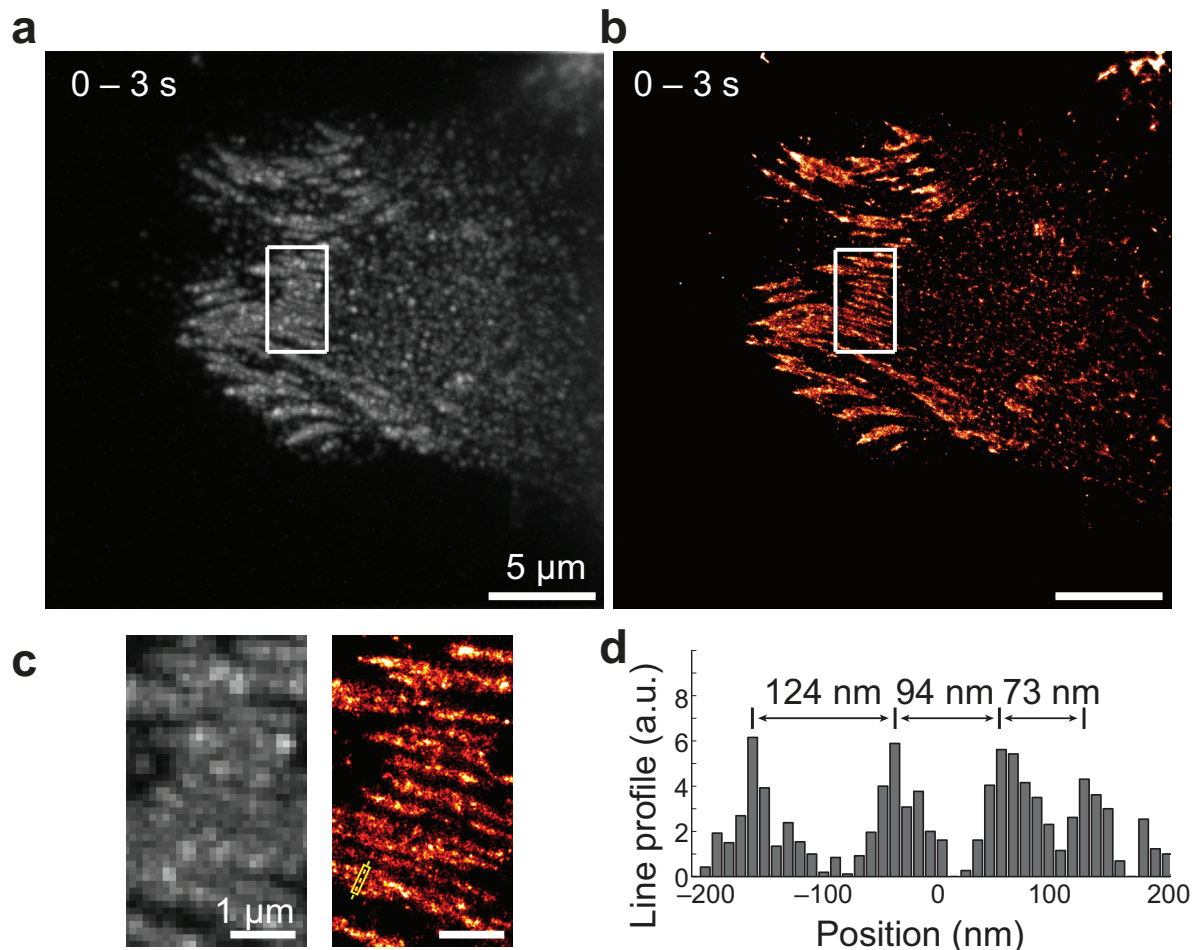
Supplementary Figure 8: Localization precision and effective photon number comparison for a single bead imaged by sCMOS and EMCCD cameras. **(a, b)** Raw EMCCD **(a)** and sCMOS **(b)** images of a 100 nm fluorescent bead. **(c, d)** Histogram of localization estimates and estimated effective photons per emitter from 800 EMCCD and sCMOS images of the same bead using conventional MLE and $\text{MLE}_{\text{sCMOS}}$, respectively (Online Methods). For EMCCD images, an effective photon conversion step is performed based on the assumption of Poisson statistics by subtracting the offset and dividing the previously characterized gain from the raw data set.⁴

Supplementary Figure 9: Localization precision histograms for Fig. 2a and Fig. 2e-g



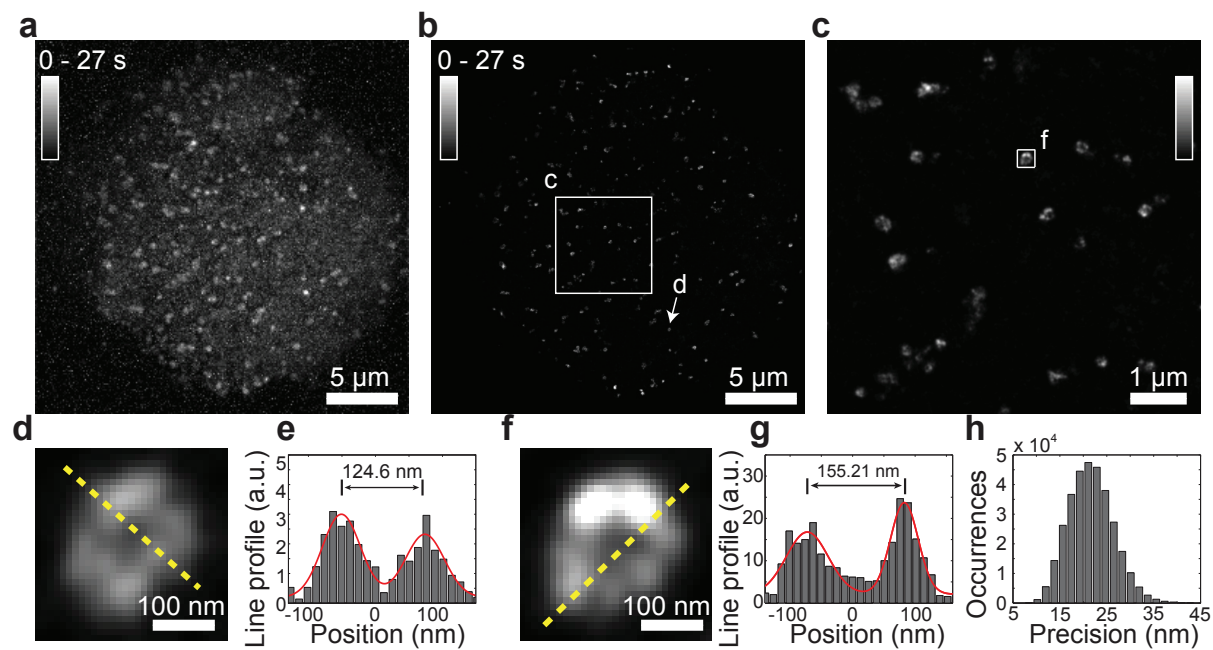
Supplementary Figure 9: Localization precision histograms for the central 256x256 pixels of the complete data set shown in Fig. 2a (**a**) and the 64x64 pixels of the entire data set shown in Fig. 2e-g (**b**). The uncertainty values in the histograms are calculated as the square root of the mean localization variance (square of localization uncertainty) in both x and y directions obtained from CRLB_{SCMOS} implemented in single-emitter fitting (**a**) and multi-emitter fitting algorithms (**b**), respectively. The mean values of the uncertainty estimates and their standard deviations are reported in the figure.

Supplementary Figure 10: Focal adhesion super-resolution image recorded in 3 seconds



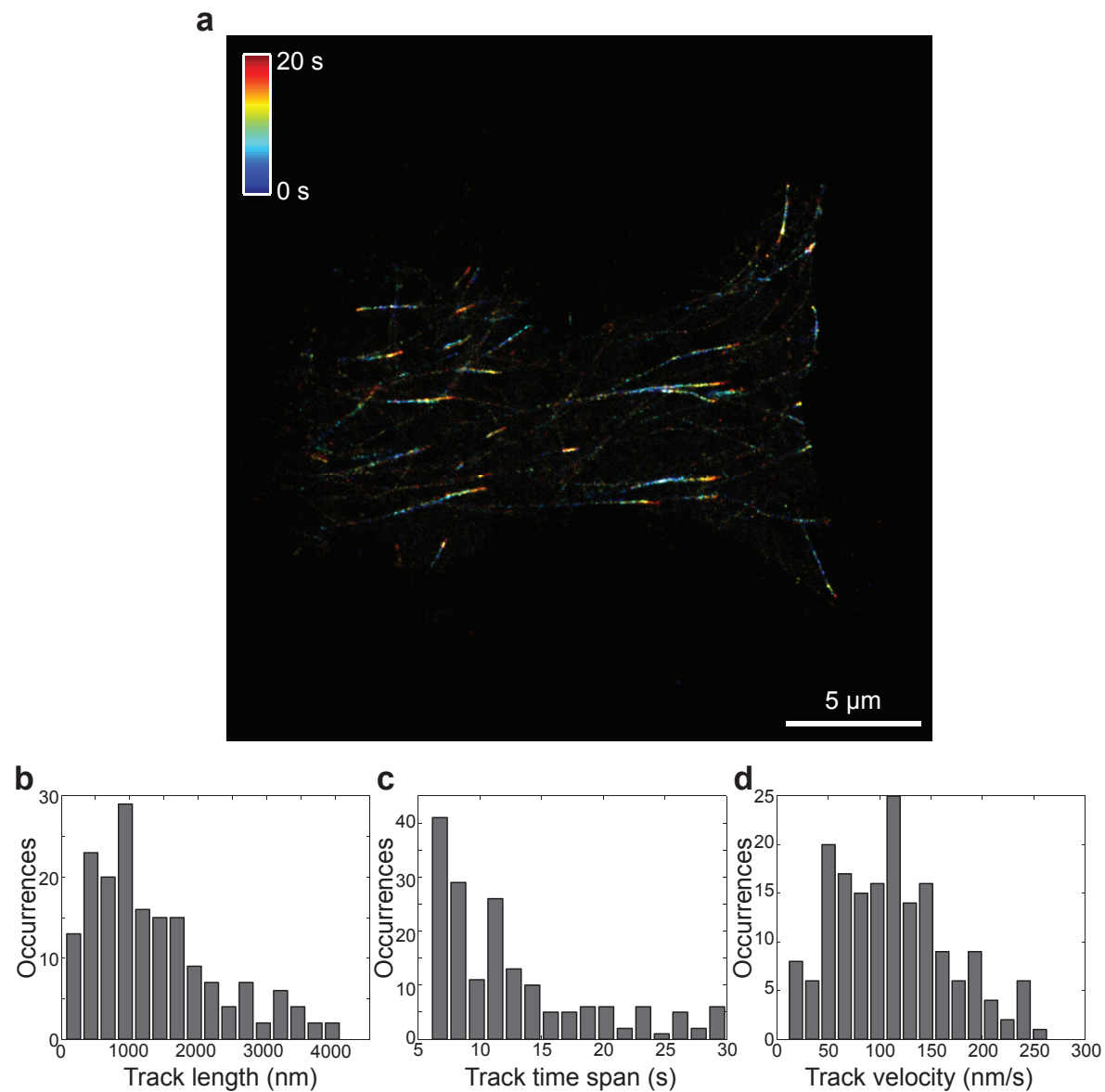
Supplementary Figure 10: Focal adhesion super-resolution image recorded in 3 seconds. (a,b) Maximum projection of a data set showing the distribution of Paxillin in focal adhesions recorded in 3 s and the corresponding super-resolution image, respectively. (c) Enlarged display of the area marked by the white boxes in (a,b). (d) Profile displaying the distribution of position estimates in the yellow box shown in the super-resolution image in (c).

Supplementary Figure 11: Super-resolution image of mEos3.2-labeled clathrin-coated pits (CCPs) in a HeLa cell



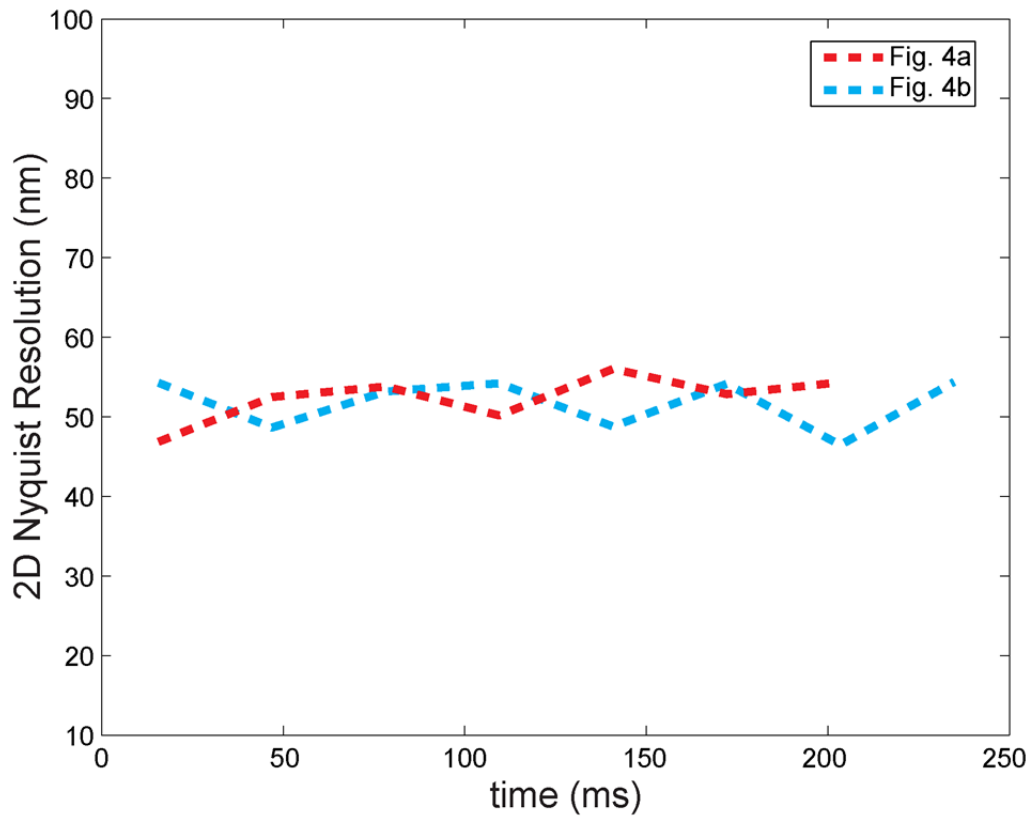
Supplementary Figure 11: Super-resolution image of mEos3.2-labeled clathrin-coated pits (CCPs) in a HeLa cell which showed little dynamics to demonstrate the achievable image quality with mEos3.2 and our sCMOS-based approach. **(a)** Maximum projection of the acquired raw data. **(b)** Super-resolution image. **(c)** Enlarged image of the area denoted by the box in **(b)**. **(d-g)** Further enlarged images **(d,f)** of the boxes in **(c)** and profiles **(e,g)** along the yellow lines in **(d,f)**. **(h)** Localization precision histogram of the data displayed in **(b)**.

Supplementary Figure 12: Super-resolution imaging of EB3-mEos3.2 in a live HeLa cell



Supplementary Figure 12: Super-resolution imaging of EB3-mEos3.2 in a live HeLa cell (Online Methods). **(a)** Super-resolution image color-coded by time demonstrating the growth of microtubule (+) ends. **(b-d)** Histograms of **(b)** track length, **(c)** track time span, and **(d)** track velocity. A total of 176 tracks were obtained from 3 data sets.

Supplementary Figure 13: Nyquist resolution measure for the 31-ms super-resolution images shown in Fig. 4



Supplementary Figure 13: Nyquist resolution measure (Online Method) for the 31-ms super-resolution images shown in Fig. 4. The Nyquist resolution is ~50 nm in all these images.

Supplementary Table

Clathrin light chain (CLC)	Sall forward: TGC AGT CGA CAT GGC TGA TGA CTT TGG CTT CTT CTC GTC BamHI reverse: CCG GTG GAT CCC TAG CGG GAC AGT GGC
EB3	BgIII forward: TCC GGA CTC AGA TCT GGC AGC GGT GGA GGC AGC GCA TCC GGC GGA AGC GGA AGC GGG GGA GCC GTC AAT GTG TAC TCC ACA TCT GTG ACC BamHI reverse: CTA GAT CCG GTG GAT CCT TAG TAC TCG TCC TGG TCT TCT TGT TGA TGC TCT TCA ATC TC
Peroxisomal membrane protein (PMP)	BgIII forward: GTC GGA AGA TCT GCC ACC ATG GCG CCG GCC GCG TCC AGG CTG C Agel reverse: ACC GGT CCG CTA CCG GAG CCG CTC TTC CCC AAG GAG GCC AGG TAG GCA TAC C
Human pyruvate dehydrogenase alpha 1 (PDHA1)	BspEI forward: GTA CAA GTC CGG AAG CGG CTC CGG GAG CGG AAG CGG GAG GAA GAT GCT CGC CGC CGT CTC BamHI reverse: CAC GTC TAG GAT CCT TAA CTG ACT GAC TTA AAC TTG ATC CAC TGA TTG GCA CCA CG

Supplementary Table: Primers used in the study.

Supplementary Note

Table of Contents

1	Photon Statistics of Cameras	18
1.1	Poisson Noise, Readout Noise and Individual Gain.....	18
1.2	EMCCD Case.....	19
1.3	sCMOS Case.....	19
2	Characterization of sCMOS Camera.....	20
2.1	Offset Characterization of sCMOS Cameras.....	20
2.2	Variance Characterization of sCMOS Cameras	20
2.3	Gain Characterization of sCMOS Cameras.....	21
3	sCMOS-specific Single-Molecule Localization Super-Resolution Algorithms	22
3.1	Image Segmentation	22
3.2	Single-Particle Localization Using $\text{MLE}_{\text{sCMOS}}$	23
3.3	Rejection Algorithm for sCMOS ($\text{LLR}_{\text{sCMOS}}$)	24
3.4	Uncertainty Estimations with $\text{CRLB}_{\text{sCMOS}}$	24
4	Analytical Approximation of the Combined Distribution Function	24
5	sCMOS Characterization Reliability Test.....	25
6	Adaptation to Weighted Least-Square Based Methods for High Photon Count Cases	26
7	Additional Discussions	27
7.1	Multi-emitter Fitting Analysis.....	27
7.2	Fast Imaging for Transferrin-Alexa Fluor 647	28
7.3	Data Analysis for High-throughput Nanoscopes.....	28
8	References.....	28

1 Photon Statistics of Cameras

In EMCCD and sCMOS cameras, imaging noise consists mainly of shot noise, thermal noise and readout noise.⁵ While shot noise stems from the photon detection process, thermal noise and readout noise originate from the electronics built around the detector chip. Reducing readout noise in sCMOS chips, which is caused by the amplification process, analog-to-digital conversion, crystal defects and contaminants in electronic devices and column-wise readout operations, has been a major focus in the improvement of the manufacturing process.⁵ However, the overall readout noise has not been reduced to a level where it can be directly and reliably applied to microscopy techniques that rely on accurate and precise localization of single molecules such as localization-based nanoscopy and single-particle tracking. On the other hand, as demonstrated in this paper, the noise pattern can be carefully characterized for each pixel and with new specifically designed localization algorithms which take this noise pattern into account, localization analysis can be performed both accurately and precisely.

1.1 Poisson Noise, Readout Noise and Individual Gain

In previously developed single-molecule localization algorithms, shot noise has been the major expected noise source and its distribution (Poisson distribution), has been included in fitting models such as the likelihood function in Maximum Likelihood Estimation (MLE)^{1,6,7}. Readout noise has not been considered in these algorithms because its presence in EMCCD cameras is small enough that it can be ignored within the tolerances of the localization precision. In the case of sCMOS cameras, however, the readout noise of each pixel is significantly higher and, in addition, every pixel has its own noise and gain characteristic with dramatic pixel-to-pixel variations (Supplementary Fig. 1).

We model the readout noise distribution for an individual pixel as a Gaussian. It describes the temporal analog-to-digital unit (ADU) count fluctuation of a single pixel with zero expected incident photons. For conciseness of the theory described below, we include the offset value for each pixel as an additive offset to the Gaussian distribution which results in a shift of the Gaussian peak. Similarly, based on the fact that each pixel has its own amplification electronics and column amplifier, gain values also vary from pixel to pixel.

When photons are detected on the sensor chip, the ADU count output of the camera follows a probability distribution which we describe here by the convolution of a Poisson distribution and a Gaussian distribution where the Poisson distribution represents the shot noise of photon detection and the Gaussian distribution is a result of the readout noise. Because of the

different characteristics of each sCMOS-pixel, each pixel has its own distinct probability density function (PDF). The PDF for an individual pixel i can be described by the following equation:

$$P_i(D) = A \sum_{q=0}^{\infty} \frac{1}{q!} e^{-u_i} u_i^q \frac{1}{\sqrt{2\pi \text{var}_i}} e^{-\frac{(D-q \cdot g_i - o_i)^2}{2\text{var}_i}} \quad (1.1)$$

Here, $P_i()$ stands for the PDF of pixel i , D represents the specific counts obtained by the camera in that pixel (in ADU), A is a normalization constant, u_i is the number of expected photoelectrons (e^-), g_i is the amplification gain (in units of ADUs/ e^-) for pixel i , and o_i and var_i stand for mean (offset) and variance of the readout noise of pixel i , respectively.

1.2 EMCCD Case

In the case of the EMCCD, where the amplification gain is large, we can examine the behavior of Eq. 1.1 in the case of small ratio var_i/g_i^2 , the exponential part on the right hand side of Eq. 1.1 becomes a delta function for an integer q . Taking into account that o_i and g_i are pixel-invariant for EMCCD cameras ($o_i = o$ and $g_i = g$, for all pixels), Eq. 1.1 can be reduced to

$$P(D_i) = A' \frac{1}{\Gamma((D_i - o)/g + 1)} e^{-u_i} u_i^{(D_i - o)/g} \quad (1.2)$$

Where A' is the normalization constant, g and o stand for the average gain and offset of the EMCCD camera and the Gamma function, $\Gamma()$, is introduced to make Eq. 1.2 compatible with non-integer values of $(D_i - o)/g$ which represents the effective photon count obtained during the preprocessing step in the analysis⁸. From Eq. 1.2, the random variable $(D_i - o)/g$ follows a Poisson distribution with mean value of u_i and Eq. 1.2 does not require $(D_i - o)/g$ to be an integer. In single-molecule localization methods developed using the MLE, Eq. 1.2 is often used as the underlying PDF to calculate likelihood functions required in both MLE and a localization uncertainty estimator using the Cramér–Rao lower bound (CRLB).

1.3 sCMOS Case

For the case of the sCMOS camera, g_i is relatively small valued (an average value of 2.13 is obtained for our camera and the average gain value of several other sCMOS camera we have tested ranged from 1.6 - 2.8 ADU/ e^- , Online Methods, Supplementary Fig. 1e,f) and the pixel variance can be significantly larger than this value (Supplementary Fig. 1a,b). Consequently,

Eq. 1.1 cannot be reduced further. A strict evaluation of the probability function can only occur numerically provided that var_i , g_i and o_i have been characterized precisely as described in this manuscript. MLE and CRLB requires evaluation of (1.1) and its first derivatives for each pixel in the fitting sub-region and potentially its second derivatives if one uses the Newton-Raphson method which has been proven to be an efficient and fast method for single molecule localization¹. These calculation burdens accumulate rapidly when applying the localization method numerically to localize millions of single molecules in order to achieve the localization density required by the Nyquist sampling theorem.

To reduce the computational complexity while still providing precise and accurate localization estimates, we describe a camera characterization method in Section 2, to obtain g_i , o_i and var_i in a reliable manner. In Section 3, we describe a set of new sCMOS-specific localization algorithms including image segmentation, localization estimation with $\text{MLE}_{\text{sCMOS}}$, a rejection algorithm with log-likelihood ratio ($\text{LLR}_{\text{sCMOS}}$) and uncertainty estimation using $\text{CRLB}_{\text{sCMOS}}$.

2 Characterization of sCMOS Camera

2.1 Offset Characterization of sCMOS Cameras

Offset values describe a constant level of ADUs pre-engineered into the readout process in order to prevent negative ADUs caused by the readout noise. The offset for each pixel is obtained by performing a temporal average on a series of images acquired in an environment with zero expected incident photons (such as putting the cap on the camera head or in a dark room). For the pixel i , the offset o_i can be calculated as

$$o_i = \frac{1}{M} \sum_{m=1}^M s_i^m \quad (2.1)$$

Here s_i^m is the ADU count at frame m for pixel i , and M is the total number of dark frames acquired.

2.2 Variance Characterization of sCMOS Cameras

The readout noise variance for each individual pixel is obtained by calculating

$$\text{var}_i = \frac{1}{M} \sum_{m=1}^M (s_i^m)^2 - o_i^2 \quad (2.2)$$

The same definitions are used as in Eq. 2.1 and var_i represents the variance of the Gaussian readout noise for pixel i .

Since the uncertainty of the variance estimates scale approximately quadratically with the underlying variance, on the order of N^2 frames are needed to achieve a similar precision as for the offset characterization with N frames. Therefore, 60,000 dark frames were taken in our experiments to precisely estimate the variance and offset of each pixel.

2.3 Gain Characterization of sCMOS Cameras

The amplification gain for each pixel of an sCMOS camera can vary significantly. To determine the gain value for each pixel we illuminated the camera with quasi-uniform stationary intensity patterns and recorded a series of image sequences (20,000 images in each sequence) at different average intensity levels ranging from ~ 20 to 200 photons per pixel. Since the Poisson distribution at these photon levels can be approximated as a Gaussian distribution, the total variance of the camera output in pixel i at a specific illumination intensity is equal to the sum of the photon shot noise-induced variance and the Gaussian variance of the specific pixel, var_i . The gain for each pixel can then be calculated with the help of the previously obtained variance var_i and offset o_i , using

$$\hat{g}_i = \arg \min \sum_{k=1}^K \left((v_i^k - \text{var}_i) - g_i (\overline{D_i^k} - o_i) \right)^2 \quad (2.3)$$

where K is the total number of illumination levels acquired for the gain calibration process, k is the k^{th} illumination sequence, $\overline{D_i^k}$ stands for the mean ADU count obtained from temporal averaging of all frames that are acquired during illumination sequence k in pixel i , o_i and var_i are the previously determined mean and variance values for pixel i , and v_i^k stands for the temporal variance of the ADU counts for illumination sequence k in pixel i .

Notice that Eq. 2.3 is a linear least square minimization problem and its equivalent matrix form can be written as

$$\hat{g}_i = \arg \min \|A_i^T - B_i^T g_i\|^2 \quad (2.4)$$

where

$$A_i = \{(v_i^1 - \text{var}_i), \dots, (v_i^k - \text{var}_i), \dots, (v_i^K - \text{var}_i)\},$$

$$B_i = \{(\overline{D_i^1} - o_i), \dots, (\overline{D_i^k} - o_i), \dots, (\overline{D_i^K} - o_i)\}$$

and $k = \{1, 2, \dots, K\}$. Using the Moore–Penrose pseudo-inverse, the gain estimate, \hat{g}_i , can be obtained using linear algebra as

$$\hat{g}_i = (B_i B_i^T)^{-1} B_i A_i^T \quad (2.5)$$

Notice that the gain obtained using this equation has the units of ADU/e⁻. The matrix representation significantly reduces the long computation time otherwise required by Eq. 2.4 for the millions of pixels of an sCMOS camera. Eq. 2.5 can be further evaluated and simplified into a single algebra equation, but since our algorithm is implemented in MATLAB the vector representation in Eq. 2.5 is sufficient and preferred. In the case of selectable gain settings for the camera, it is important to make sure that the gain setting used in calibration matches the gain setting used in the biological imaging.

3 sCMOS-specific Single-Molecule Localization Super-Resolution Algorithms

3.1 Image Segmentation

As the first step in localization-based super-resolution^{9–13} analysis, image segmentation is performed with the help of various smoothing filters to eliminate the noisy peaks caused by Poisson noise and the heterogeneous background fluorescence. Uniform filters and Gaussian filters can be used as fast and efficient smoothing filters in the image segmentation step. Although these algorithms have proven their efficiency for super-resolution imaging with EMCCD cameras, their performance is not ideal when applied to the case of sCMOS cameras. Readout noise and pixel-dependent gain in sCMOS cameras introduce large numbers of random peaks in the raw images. High-noise pixels cannot easily be eliminated without specific knowledge of the camera. Here, we have developed a segmentation algorithm that takes advantage of the information we obtained in the characterization step above and thus provides a reliable way of performing image segmentation for sCMOS cameras.

First, similar to a method previously described⁸, the segmentation algorithm applies two uniform filters with different kernel sizes to reduce noise from various sources. For the sCMOS camera, we additionally take advantage of the pixel-dependent noise and gain characteristics in the kernel function. The new variance-gain varied uniform filter is defined as,

$$unif(D_i, n) = \frac{\sum_{i \in C_{n \times n}} \left[\frac{(D_i - o_i)}{g_i \text{ var}_i} \right]}{\sum_{i \in C_{n \times n}} \text{var}_i^{-1}} \quad (3.1)$$

Where D_i is the ADU count in an sCMOS-aquired image for pixel i , g_i and var_i are the previously obtained characterization parameters, and $C_{n \times n}$ represents the kernel region which in this case is a $n \times n$ square box centered around pixel i . A smoothed image S_1 is obtained by performing a pixel-wise subtraction between two images resulting from two uniform filter applications with different kernel sizes n :

$$S_1 = unif(D, \lfloor 2\sigma_{PSF} + 1 \rfloor) - unif(D, \lfloor 4\sigma_{PSF} + 1 \rfloor) \quad (3.2)$$

Here $\lfloor x \rfloor$ describes the largest integer less than or equal to x , D represents the entire image. Based on this smoothed image, local maxima can then be found using a maximum filter routine and a binary operation⁸. These operations are designed to be fast and efficient in order to shorten the analysis time.

3.2 Single-Particle Localization Using MLE_{sCMOS}

As an alternative to numerically evaluating the full likelihood function for sCMOS cameras as described by Eq. 1.1, we developed an analytical approximation that greatly simplifies the calculation while providing optimal accuracy and precision at the theoretical limit (Fig. 1c,d and Supplementary Fig. 3). The analytical approximation for Eq. 1.1 can be described as

$$P_{scmos}(x = [(D_i - o_i)/g_i + \text{var}_i/g_i^2] | u_i, \text{var}_i, g_i, o_i) = \frac{e^{-(\mu_i + \text{var}_i/g_i^2)} (\mu_i + \text{var}_i/g_i^2)^x}{\Gamma(x+1)} \quad (3.3)$$

Where μ_i stands for the expected photons from the fitting model (single 2D Gaussian model for single emitter fitting and multiple Gaussian model from multi-emitter fitting) at pixel i (see Section 4 for steps in obtaining this approximation). Thus, the MLE can be expressed using $P_{scmos}(x = [(D_i - o_i)/g_i + \text{var}_i/g_i^2] | u_i, \text{var}_i, g_i, o_i)$ as

$$\hat{\theta} = \arg \min_{\theta} \left\{ -\ln \left[\prod_{i=1}^M P_{scmos}(x = [(D_i - o_i)/g_i + \text{var}_i/g_i^2] | u_i(\theta), bg, \text{var}_i, g_i, o_i) \right] \right\} \quad (3.4)$$

where $\hat{\theta}$ is the maximum likelihood estimate for parameter set θ and M is the total number of pixels in the fitting sub-region.

Since the new analytical expression of the likelihood function resembles a Poisson distribution, it is then convenient to directly implement this new probability distribution in an established MLE method^{1,6–8,14,15} and multi-emitter fitting type of analysis where a Poisson noise model is expected^{8,16,17}.

3.3 Rejection Algorithm for sCMOS (LLR_{sCMOS})

A rejection algorithm (goodness of fit filtering) is essential for removing non-convergent fits, and sub-regions that contains more than the allowable number of emitters (1 for single emitter fitting, n for multi-emitter fitting). The Log-likelihood ratio (LLR) metric¹⁸ provides a consistent and unbiased rejection behavior. LLR_{sCMOS} can be written as:

$$LLR_{sCMOS} = -2 \ln \left(\prod_{i=1}^M \frac{P_{sCMOS}(x = [(D_i - o_i)/g_i + \text{var}_i/g_i^2] | u_i(\theta), bg, \text{var}_i, g_i, o_i)}{P_{sCMOS}(x = [(D_i - o_i)/g_i + \text{var}_i/g_i^2] | (D_i - o_i)/g_i, bg, \text{var}_i, g_i, o_i)} \right) \quad (3.5)$$

LLR_{sCMOS} approximately follows a χ^2 distribution with $M-K$ degrees of freedom where M is the number of pixels in the fitting sub-region and K is the total number of parameters estimated in the fitting process. Thus, the p-value can be calculated for each fit followed by a thresholding process to reject fits with p-values below a certain predetermined level.

3.4 Uncertainty Estimations with CRLB_{sCMOS}

Uncertainty estimates can be approximated using the CRLB with the sCMOS-likelihood function of Eq. 3.3. As described similarly in previous publications^{1,8}, each element of the Fisher information matrix can thus be expressed as

$$I_{i,j}(\theta) = \sum_{k=1}^M \frac{1}{\mu_k + \frac{\text{var}_k}{g_k^2}} \frac{\partial \mu_k(\theta)}{\partial \theta_i} \frac{\partial \mu_k(\theta)}{\partial \theta_j} \quad (3.6)$$

where μ_k is the expected photon count coming from the fitting model at pixel k and $\theta = \{\theta_1, \theta_2, \dots, \theta_n\}$ are the obtained estimates from the fitting with MLE_{sCMOS}. The CRLB_{sCMOS} is obtained by calculating the inverse of $I(\theta)$.¹⁹

4 Analytical Approximation of the Combined Distribution Function

An equivalent expression of the combined distribution in Eq. 1.1 is given by

$$P_i(D) = A \sum_{q=0}^{\infty} \frac{1}{q!} e^{-\mu_i} \mu_i^q \frac{1}{\sqrt{2\pi \text{var}_i}} e^{-\frac{[(D-o_i)/g_i-q]^2}{2\text{var}_i/g_i^2}} \quad (4.1)$$

Thus, the distribution of the random variable $(D-o_i)/g_i$ can be directly expressed as a convolution between two distributions, a Poisson distribution $P(\mu_i)$ and a Gaussian distribution with zero mean and variance of var_i/g_i^2 , $G(0, \text{var}_i/g_i^2)$. Therefore, adding a pixel-dependent constant, var_i/g_i^2 , to the random variable, the distribution of $(D-o_i)/g_i + \text{var}_i/g_i^2$ becomes

$$(D-o_i)/g_i + \text{var}_i/g_i^2 \sim P(\mu_i) \otimes G(\text{var}_i/g_i^2, \text{var}_i/g_i^2) \quad (4.2)$$

Since $G(\text{var}_i/g_i^2, \text{var}_i/g_i^2)$ asymptotically approaches $P(\text{var}_i/g_i^2)$, we can approximate it with $P(\text{var}_i/g_i^2)$. Furthermore, since the convolution of two Poisson distributions with expected values a and b is equal to a Poisson distribution with an expected value of $a+b$, we arrive at our analytical approximation of Eq. 1.1 as

$$(D-o_i)/g_i + \text{var}_i/g_i^2 \sim P(\mu_i + \text{var}_i/g_i^2) \quad (4.3)$$

The quality of the approximation in various imaging and camera conditions can be quantified by calculating the Komogorov distance²⁰, i.e. the maximum absolute difference between the cumulative distribution functions based on the approximation and the original distribution described by Eq. 1.1. Supplementary Fig. 3 shows the dramatic improvement of the Komogorov distance (up to one order of magnitude) of our approximation compared to the Komogorov distance between a Poisson distribution and the original distribution described by Eq. 1.1. As shown in Fig. 1c,d our approximation leads to accurate and precise localization results at the theoretical limit.

5 sCMOS Characterization Reliability Test

We confirmed that the determined pixel-specific parameters do not change significantly over time in a typical lab environment. However, a slight change in the characteristics of our sCMOS camera was detected when switching cooling of the camera from fan to liquid cooling which caused a change in operation temperature of around 30 kelvins. Since this temperature can also change with ambient temperature and humidity, special care should be used when such changes are expected.

To test whether the determined values o_i and var_i can describe the current state of the camera, we developed a test method based on the concept of p-value testing.

A test sequence of dark images was first recorded as described in section 2.1. This sequence does not need to be as long as the dark sequence used to characterize the camera (1,000 frames are sufficient). If the characteristics of the camera have not changed significantly since the previous characterization date, the test sequence should be a random subset drawn from the Gaussian distribution described by the previously determined o_i and var_i values. Thus, the log-likelihood ratio statistics should follow a χ^2 distribution with K degrees of freedom.¹⁸ The p-value of the log-likelihood ratio statistics in the case of a Gaussian distribution can be calculated as

$$p_i = 1 - \chi_{CDF}^2(K, \sum_{j=1}^K \frac{(D_i^j - o_i)}{\text{var}_i}) \quad (5.1)$$

where p_i is the p-value for pixel i , D_i^j is the output ADU counts at frame j of the test sequence at pixel i , K is the total number of frames in the test sequence and $\chi_{CDF}^2(K, x)$ is the cumulative distribution function of a Chi-square distribution with K degrees of freedom.

In theory, the resulting p-values from every tested pixel should follow a uniform distribution ranging from 0 to 1. However, because of the estimation uncertainties in the previous characterization step, the resulting p-value distribution deviates from a uniform distribution into a valley shaped distribution where both tails near 0 and 1 are significantly higher than the middle part of the distribution. Considering that the environmental change is expected to result in a global change of a certain parameter across the whole chip, such as an increase in the variances of all pixels, the resulting p-value distribution will shift towards one tail or the other. We therefore conclude that if the mean of the obtained p-values is close to 0.5 (± 0.1 ; this value also depends on the uncertainty in the characterization step) indicating a symmetric p-value distribution, the previous parameters are still valid.

6 Adaptation to Weighted Least-Square Based Methods for High Photon Count Cases

Since the performance of the weighted Least-Square Estimator (wLSE) asymptotically approaches MLE with increasing number of detected photons⁷, one could also use wLSE to obtain accurate single molecules localizations in high photon count situations using sCMOS cameras. When the number of detected photons in pixel i is large, we approximate the Poisson distribution as a Gaussian, $P(\mu_i) \sim G(\mu_i, \mu_i)$, and therefore Eq. 4.1 reduces to a convolution between two Gaussians. Thus

$$(D - o_i) / g_i \sim G(\mu_i, \mu_i) \otimes G(0, \text{var}_i / g_i^2) \quad (6.1)$$

The distribution of $(D - o_i) / g_i$ can then be expressed as a single Gaussian distribution,

$$(D - o_i) / g_i \sim G(\mu_i, \mu_i + \text{var}_i / g_i^2) \quad (6.2)$$

Finally, we arrive at the expression of $w\text{LSE}_{\text{scmos}}$ for high photon count cases,

$$\hat{\theta}_{w\text{LSE}} = \arg \min_{\theta} \left\{ \sum_i^K \frac{((D - o_i) / g_i - \mu_i)^2}{\mu_i + \text{var}_i / g_i^2} \right\} \quad (6.3)$$

7 Additional Discussions

7.1 Multi-emitter Fitting Analysis

The general principle of multi-emitter fitting methods^{8,16,17,21,22} is to simultaneously infer multiple single molecule center locations (or localization probabilities distributions) while their Point Spread Functions (PSFs) partially overlap. A theoretical study²³ has predicted that in comparison to single-emitter fitting a 7-fold improvement of speed in achieving the same localization density is expected when algorithms can fit up to 5 emitters per sub-region. However, there is a limit of how many molecules can be fitted for each sub-region before it starts to compromise the localization precision. Since with increasing numbers of molecules per area, the information contained in each sub-region stays the same, the fixed amount of information is then shared between all molecules in the fitting sub-region and the localization precision will decrease with increasing number of molecules. In the authors' experience, multi-emitter fitting up to 8-10 emitters per μm^2 does not severely compromise the localization precision⁸. This can be partially illustrated by the correlation coefficient map in Supplementary Fig. 4c-d which shows that not every pixel within the sub-region shares the same influence on the localization estimate and thus fitting multiple emitters within the sub-region helps to take full advantage of the information within. At the same time, uncertainties of the estimates can be accurately predicted by $\text{CRLB}_{\text{scmos}}$ (CRLB). This provides a way to filter out low localization precision estimates in the multi-emitter fitting analysis. A consistent and statistically meaningful rejection algorithm is also critical to filter out non-converging fits since the fitting complexity increases dramatically with increasing numbers of emitters considered in the fitting process.

7.2 Fast Imaging for Transferrin-Alexa Fluor 647

The fast imaging of transferrin-Alexa Fluor 647 was performed with an imaging buffer containing 2-mercaptoethanol and an oxygen scavenging system. The removal of oxygen and the presence of thiols (2-mercaptoethanol and endogenous thiols such as glutathione) promotes conversion of the dye triplet state to the dark dye-thiol adduct²⁴ of the blinking cycle over quenching by triplet oxygen back to the ground state with concurrent production of reactive singlet oxygen. The reaction between the thiol and the dye may proceed through the formation of thiyl radicals by electron transfer from the thiol anion to the cyanine dye before bond formation²⁵; the quenching of the thiyl radical by reaction with the cyanine is consistent with the fact that the imaging conditions were not observed to affect normal cell morphology over the course of imaging (about 10 s for transferrin and up to 2 minutes for the other live cell data) in our live-cell experiments which is in agreement with previous reports²⁶.

Additionally, the laser intensities in the sample are far below values reported for other live-cell imaging techniques such as multiphoton microscopy²⁷ or fluorescence recovery after photobleaching.

7.3 Data Analysis for High-throughput Nanoscopes

The benefits of faster and more sensitive imaging of large FOVs are crucial for the development of high-throughput nanoscopy. Using the method presented here, the data post-processing time (despite the GPU implementation) still greatly exceeds the time to record the raw data. The main limitation is the time to retrieve the raw data from mass storage devices (in this case, RAID0 array of four solid state drives). However, similar to other high-throughput approaches, archiving camera raw data is arguably not a necessary requirement anymore given the reliable and statistics-based performance of our algorithms. Feeding the camera data directly into the GPU memory while it is recorded and taking advantage of full parallel implementation and the dynamic parallelism technique can therefore remove this bottle neck, paving the way for a new generation of high-throughput nanoscopes.

8 References

1. Smith, C. S., Joseph, N., Rieger, B. & Lidke, K. A. Fast, single-molecule localization that achieves theoretically minimum uncertainty. *Nature Methods* **7**, 373–5 (2010).
2. Rodgers, J. L. & Nicewander, W. A. Thirteen Ways to Look at the Correlation Coefficient. *The American Statistician* **42**, 59–66 (1988).

3. Fixman, M. Polymer conformational statistics. III. Modified Gaussian models of stiff chains. *The Journal of Chemical Physics* **58**, 1564 (1973).
4. Lidke, K. A., Rieger, B., Lidke, D. S. & Jovin, T. M. The role of photon statistics in fluorescence anisotropy imaging. *IEEE Transactions on Image Processing* **14**, 1237–45 (2005).
5. Tian, H. Noise Analysis in CMOS Image Sensors. *Ph.D. Thesis, Stanford University* 1–101 (2000).
6. Ober, R. J., Ram, S. & Ward, E. S. Localization accuracy in single-molecule microscopy. *Biophysical Journal* **86**, 1185–1200 (2004).
7. Mortensen, K. I., Churchman, L. S., Spudich, J. A. & Flyvbjerg, H. Optimized localization analysis for single-molecule tracking and super-resolution microscopy. *Nature Methods* **7**, 377–81 (2010).
8. Huang, F., Schwartz, S. L., Byars, J. M. & Lidke, K. A. Simultaneous multiple-emitter fitting for single molecule super-resolution imaging. *Biomedical Optics Express* **2**, 1377–93 (2011).
9. Betzig, E. *et al.* Imaging intracellular fluorescent proteins at nanometer resolution. *Science (New York, N.Y.)* **313**, 1642–5 (2006).
10. Rust, M. J., Bates, M. & Zhuang, X. W. Sub-diffraction-limit imaging by stochastic optical reconstruction microscopy (STORM). *Nature Methods* **3**, 793–5 (2006).
11. Hess, S. T., Girirajan, T. P. K. & Mason, M. D. Ultra-high resolution imaging by fluorescence photoactivation localization microscopy. *Biophysical Journal* **91**, 4258–72 (2006).
12. Heilemann, M. *et al.* Subdiffraction-resolution fluorescence imaging with conventional fluorescent probes. *Angewandte Chemie International Edition* **47**, 6172–76 (2008).
13. Fölling, J. *et al.* Fluorescence nanoscopy by ground-state depletion and single-molecule return. *Nature Methods* **5**, 943–5 (2008).
14. Quan, T. *et al.* Ultra-fast, high-precision image analysis for localization-based super resolution microscopy. *Optics Express* **18**, 11867–76 (2010).
15. Ram, S., Prabhat, P., Ward, E. S. & Ober, R. J. Improved single particle localization accuracy with dual objective multifocal plane microscopy. *Optics Express* **17**, 6881–98 (2009).
16. Holden, S. J., Uphoff, S. & Kapanidis, A. N. DAOSTORM: an algorithm for high-density super-resolution microscopy. *Nature Methods* **8**, 279–80 (2011).
17. Mukamel, E. A., Babcock, H. & Zhuang, X. Statistical deconvolution for superresolution fluorescence microscopy. *Biophysical Journal* **102**, 2391–400 (2012).
18. Wilks, S. S. The Large-Sample Distribution of the Likelihood Ratio for Testing Composite Hypotheses. *The Annals of Mathematical Statistics* **9**, 60–62 (1938).

19. Kay, S. M. *Fundamentals of Statistical Signal Processing, Volume I: Estimation Theory* (v. 1). 625 (Prentice Hall: 1993).
20. Kolmogorov, A. Sulla Determinazione Empirica di una Legge di Distribuzione. *Giornale dell'Istituto Italiano degli Attuari* **4**, 83–91 (1933).
21. Quan, T. *et al.* High-density localization of active molecules using Structured Sparse Model and Bayesian Information Criterion. *Optics Express* **19**, 16963–74 (2011).
22. Cox, S. *et al.* Bayesian localization microscopy reveals nanoscale podosome dynamics. *Nature Methods* **9**, 195–200 (2012).
23. Small, A. R. Theoretical Limits on Errors and Acquisition Rates in Localizing Switchable Fluorophores. *Biophysical Journal* **96**, L16–L18 (2009).
24. Van de Linde, S. *et al.* Direct stochastic optical reconstruction microscopy with standard fluorescent probes. *Nature Protocols* **6**, 991–1009 (2011).
25. Dempsey, G. T. *et al.* Photoswitching mechanism of cyanine dyes. *Journal of the American Chemical Society* **131**, 18192–3 (2009).
26. Jones, S. A., Shim, S.-H., He, J. & Zhuang, X. Fast, three-dimensional super-resolution imaging of live cells. *Nature Methods* **8**, 499–505 (2011).
27. Koester, H. J., Baur, D., Uhl, R. & Hell, S. W. Ca²⁺ fluorescence imaging with pico- and femtosecond two-photon excitation: signal and photodamage. *Biophysical Journal* **77**, 2226–36 (1999).